A Three Switch Resonant Inverter for Multiple Load Induction Heating Applications

Bhavin Salvi, S. Porpandiselvi, *Member, IEEE*, and N. Vishwanathan

***Abstract*—Induction heating (IH) is a trending technology in the domestic applications due to its advantages related to high efficiency, better control, and fast heating. Present research focuses on developing cost-effective and highly efficient solutions. In this article, a three-switch inverter (3SI) for multiple load IH applications is proposed, which meets previous requirements. Reduced component count and high efficiency are the key benefits of the proposed inverter. Asymmetric duty cycle control is used to obtain independent control over two loads simultaneously. The operation of the proposed 3SI has been verified by rigorous simulations in Orcad PSpice software and by experimenting with designed hardware prototype. The simulation and experimental results are in good agreement with each other, proving the proposed 3SI as a feasible solution for multiple load IH applications.**

***Index Terms*—Induction heating (IH), multiple load, reduced component count, soft switching, three-switch inverter (3SI).**

I. Introduction

INDUCTION cookers are gaining popularity in the market for its high efficiency, safety, cleanliness, and fast heating over traditional heating techniques [1]. Due to high-frequency ac supply, eddy currents are generated in the heating load at a skin depth level from surface. Skin depth (δ) is defined as

$$\delta = \sqrt{\frac{\rho}{\pi \mu f_s}}$$

where ρ is resistivity of the material, f_s is the operating frequency of inverter, and μ is magnetic permeability of the material.

In induction cooking application, high-frequency (20–30 kHz) ac input is required. As low-frequency ac input is commonly available, it is rectified and then converted into high-frequency ac, which is suitable for induction heating (IH) application. The higher efficiency of resonant inverters makes them suitable for this purpose. Most commonly, full-bridge [2], half-bridge [3], [4], and single-switch [5] resonant inverter configurations are used for IH applications. Single-switch configurations are suitable for low-power, low-cost applications. Half-bridge and full-bridge configurations are suitable for medium- and high-power applications, respectively. For power control in IH applications, square wave control [6], asymmetrical control [2], [7], [8], pulse density modulation [9], [10], and phase-shift control [11] are frequently used.

In induction cooking, there is a requirement of heating multiple loads at a time. For this, various multiload configurations have been proposed in the past. Low component count, higher efficiency, and independent control of load are key objectives in designing multiload topologies. Master–slave load approach is used to control power by frequency variation and capacitor switching [12]. This requires higher number of capacitors and electromechanical switches. Acoustic noise and electromagnetic interference problems may arise due to the usage of electromechanical switches and control by varying frequency. An inverter topology using nine switches for two three-phase loads has been proposed in [13]. Pulsewidth modulation technique is used for the independent control of two motors. A topology for two loads, which reduces one leg from conventional full-bridge approach, is presented in [14]. Same topology has been extended for three loads in [15]. This three-leg inverter is used for multiload application with suitable control technique in [16]. However, fully independent control is not possible as control of loads is related with each other to some extent. By using a common capacitor for two loads, a topology with less component count is presented in [17]. A two-output three-level converter is proposed [18] to reduce voltage stresses across the switches. Dual frequency inverter for multiple loads is proposed in [19]. The dual-frequency inverter is suitable for heating vessels of different materials but soft switching of switches is affected due to two frequency approach.

In this article, an inverter is proposed to meet all the key requirements for multiple load IH systems. It uses three switches to power two loads. These loads are simultaneously and independently controlled with simple asymmetrical duty cycle control technique. The proposed inverter can be extended for multiple load applications. The extended configuration is suitable for heating IH loads of ferromagnetic and nonferromagnetic materials simultaneously and independently.

The rest of this article is organized as follows. Section II details the proposed inverter and it is different operating modes. Section III comprises of the analysis and derivation of equations related to the inverter output power. Section IV shows the detailed efficiency analysis of the inverter. Section V focuses on simulation, experimental setup, and experimental results of the inverter. Extension of the proposed inverter for multiple loads

Manuscript received February 1, 2022; revised April 5, 2022; accepted May 4, 2022. Date of publication May 10, 2022; date of current version June 24, 2022. Recommended for publication by Associate Editor L. Zhang.*(Corresponding author: Bhavin Salvi.)*

The authors are with the Department of Electrical Engineering, National Institute of Technology Warangal, Warangal 506004, India (e-mail: sbhavin@student.nitw.ac.in; selvi@nitw.ac.in; nvn@nitw.ac.in).

Color versions of one or more figures in this article are available at https://doi.org/10.1109/TPEL.2022.3173931.

Digital Object Identifier 10.1109/TPEL.2022.3173931

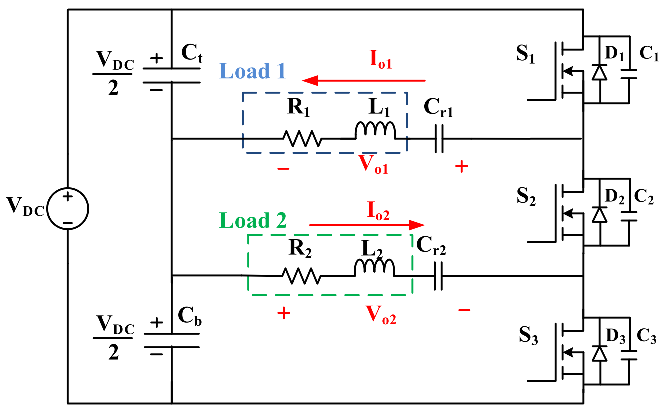

Fig. 1. Proposed 3SI configuration.

is discussed in Section VI. Finally, Section VII concludes this article.

II. Proposed Three-Switch Inverter (3SI)

Fig. 1 shows the proposed 3SI configuration for multiple load IH applications. A dc source V_{dc} with two split capacitors, supplies power to two IH loads (Load-1 and Load-2) through three MOSFETs (S_1, S_2, and S_3). An IH load is modeled as series combination of *RL*. Load-1 is modeled as R_1 and L_1, and load-2 is modeled as R_2 and L_2. Resonant capacitors C_{r1} and C_{r2} are placed to resonate load-1 and load-2, respectively. Values of resonant capacitors are selected such that both loads will operate in a slightly inductive mode to ensure zero voltage switching (ZVS) operation. V_{01}, I_{o1} and V_{o2}, I_{o2} are output voltages and currents for load-1 and load-2, respectively. Conventions of currents and voltages indicated in Fig. 1 are taken as the reference.

Fig. 3 shows the waveforms of the switching pulses of devices S_1, S_2, and S_3 (V_{g1}, V_{g2}, and V_{g3}, respectively) and output voltages. V_{g2} is generated by logical EX-OR of V_{g1} and V_{g3}. Fig. 2 shows different operating modes of the proposed 3SI.

A. Mode-1 ($0 - t_1$)

As shown in Fig. 3, S_2 and S_3 switches are ON and switch S_1 is OFF in this mode. Voltage across S_1 in its OFF state is V_{dc}. S_3 is being turned ON from Mode-3 to Mode-1. Negative current flowing through body diode D_3 ensures ZVS during turn-ON of S_3. Bottom capacitor (C_b) in split capacitor arrangement powers both the IH loads in this mode. Load-1 current flows through switches S_2 and S_3, whereas load-2 current flows through switch S_3 only. Flow of currents through the loads is shown in Fig. 2.

B. Mode-2 ($t_1 - t_2$)

In this mode, switches S_1 and S_3 are ON and S_2 is OFF. The voltage across S_2 in its OFF state is V_{dc}. S_1 is being turned ON from Mode-1 to Mode-2. Freewheeling of load-1 current through body diode D_1 assures ZVS turn-ON of S_1. Both the loads are powered by top (C_t) and bottom (C_b) split capacitors, respectively. Load-1 output voltage polarity and current direction reverses, whereas load-2 output voltage polarity and current direction remains the same as Mode-1. Flow of currents through the loads is shown in Fig. 2.

C. Mode-3 ($t_2 - T$)

In this mode, switches S_1 and S_2 are ON and S_3 is OFF. Top capacitor powers both the IH loads. The voltage across S_1 in its OFF state is V_{dc}. S_2 is being turned ON from Mode-2 to Mode-3. ZVS during turn-ON of S_3 is ensured as the negative current flows through body diode D_3. Top capacitor (C_t) in split-capacitor arrangement powers both the IH loads. Load-1 and load-2 currents flow through switches S_1 and S_2, respectively. Load-2 output voltage polarity and current direction is reversed in this mode. The flow of currents through the loads is shown in Fig. 2.

III. Output Power Calculations

By doing Fourier analysis on the output load voltage waveform depicted in Fig. 4, the expression for output voltage is obtained as follows:

$$v_o(t) = \frac{V_{dc}(2d-1)}{2} + \sum_{n=1}^{\infty} \frac{2V_{dc}}{n\pi} \sin(n\pi d)\cos(n\omega t - n\pi d) \tag{1}$$

where $d = \frac{t_{on}}{T}$, t_{on} is the ON time period of the switching devices, and $0.5 \leq d < 1$. The fundamental voltage component is

$$v_{o1}(t) = \frac{2V_{dc}}{\pi} \sin(\pi d)\cos(\omega t - \pi d). \tag{2}$$

Peak and root mean square (rms) output voltages can be expressed as follows:

$$V_m = \frac{2V_{dc}}{\pi} \sin(\pi d) \tag{3}$$

$$V_{rms} = \frac{\sqrt{2}V_{dc}}{\pi} \sin(\pi d). \tag{4}$$

Now, fundamental current can be derived as follows:

$$i_o = I_m \sin(\omega t - \pi d - \psi) \tag{5}$$

where I_m is the peak current and ψ is the phase angle between current and voltage. Now, $I_m = \frac{V_m}{|Z|}$, where $Z = R + j\omega L - \frac{j}{\omega C}$ = impedance of the load. Resistive part of the load $R = |Z|\cos\psi$ and inductive part of the load $X = |Z|\sin\psi$, and

$$\cos\psi = \frac{1}{\sqrt{1 + Q_L^2(\frac{\omega}{\omega_o} - \frac{\omega_o}{\omega})^2}} \tag{6}$$

where Q_L = quality factor of the load and ω_o = resonant frequency. Load rms current can be derived as follows:

$$I_{o,rms} = \frac{\sqrt{2}V_{dc}\sin(\pi d)}{\pi}\frac{\cos\psi}{R}. \tag{7}$$

Now, output load power, $P_o = I_{o,rms}^2 R_i$. Hence,

$$P_o = \frac{2V_{dc}^2 \sin^2(\pi d)}{\pi^2 R^2} \times \frac{R_i}{1 + Q_L^2(\frac{\omega}{\omega_o} - \frac{\omega_o}{\omega})^2} \tag{8}$$

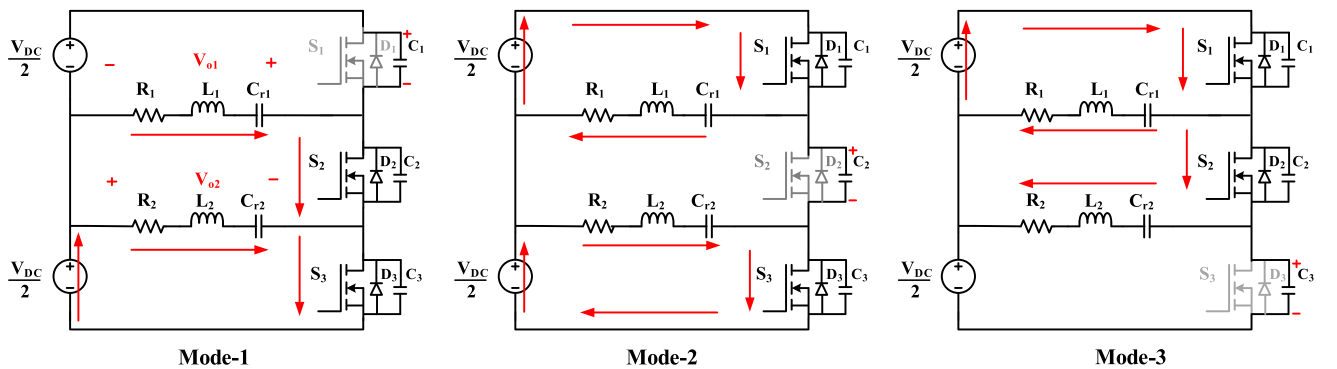

Fig. 2. Modes of operation.

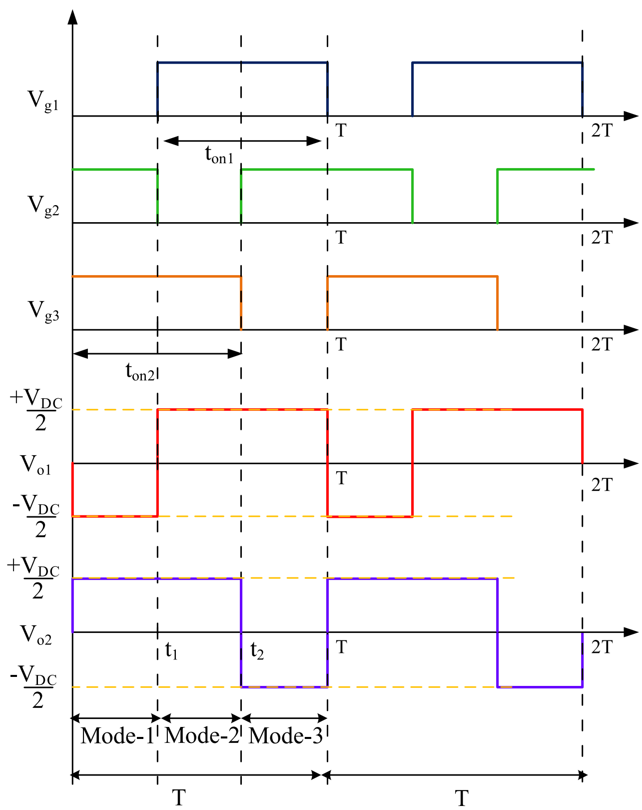

Fig. 3. Proposed 3SI waveforms. From top to bottom: gate pulses, load-1 output voltage (V_{o1}) and load-2 output voltage (V_{o2}).

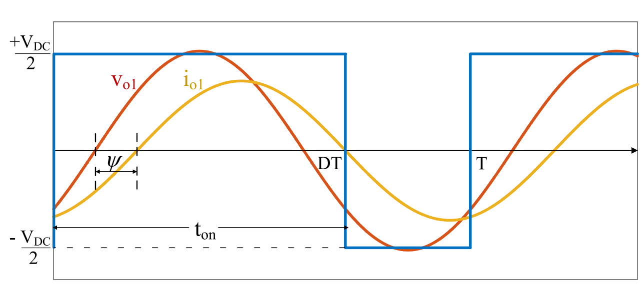

Fig. 4. Output voltage–current waveform.

where $R = R_i + r_{\rm DS} + r_L + r_C$, R_i is the effective resistance of IH load, $r_{\rm DS}$ is average equivalent ON state resistance of MOSFET, and r_L and r_C are parasitic resistances offered by inductor and capacitor, respectively.

The proposed 3SI must be operated with $t_{\rm on}$ greater than $|T/2|$ with asymmetric duty cycle (ADC) control. So duty cycle for control is defined as follows:

$$D = \frac{T - t_{\rm on}}{T/2} \tag{9}$$

where $t_{\rm on}$ is ON time duration of the switch, which is greater than $|T/2|$. Duty cycles D_1 and D_2 are obtained for switches S_1 and S_3 using the following expression :

$$D_1 = \frac{T - t_{\rm on1}}{T/2} \tag{10}$$

$$D_2 = \frac{T - t_{\rm on2}}{T/2}. \tag{11}$$

The control over load-1 and load-2 power is obtained by varying D_1 and D_2, respectively. The change in IH load rms currents over duty cycle is as per Fig. 5. Fig. 5(a) depicts the change in load rms currents when D_1 is varied by keeping D_2 at 99%. Fig. 5(b) shows the change in load rms currents when D_2 is varied by keeping D_1 at 99%.

IV. Efficiency Analysis

For the proposed 3SI, the efficiency(η) can be obtained as the ratio between its output to input power. Output power is the net power delivered to the load after losses. Losses in the inverter can be categorized as conduction losses $P_{\rm con}$ and switching losses $P_{\rm sw}$.

$$\eta = \frac{P_o}{P_{\rm in}} = \frac{P_{\rm in} - P_{\rm losses}}{P_{\rm in}} = \frac{P_{\rm in} - (P_{\rm con} + P_{\rm sw})}{P_{\rm in}}. \tag{12}$$

A. Conduction Losses

Conduction losses are the summation of the losses in the switching devices ($P_{\rm con,sw}$), losses in the resonant capacitors ($P_{\rm con,rc}$), and losses in the IH coil ($P_{\rm con,coil}$).

1) Conduction Losses in Switches: The current flowing through the switches is part of the load currents. Expressions

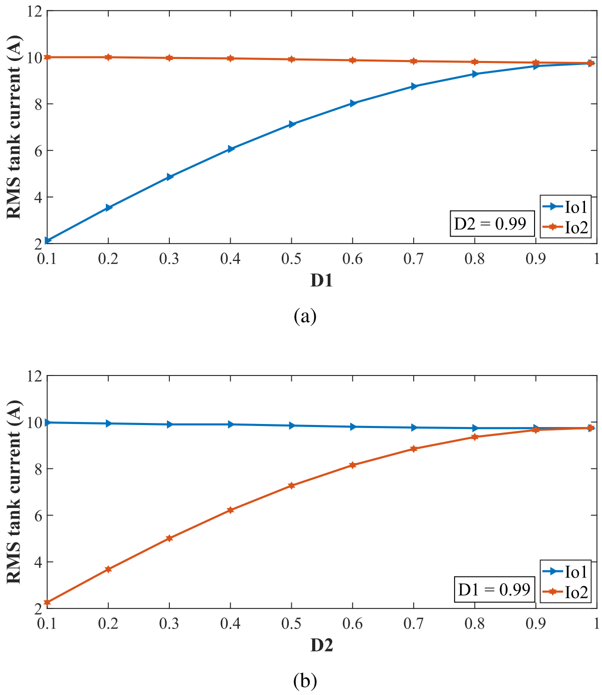

Fig. 5. Variation of rms tank current with duty cycle. (a) D_1 varied with D_2 constant at $D_{2\max}$. (b) D_2 varied with D_1 constant at $D_{1\max}$.

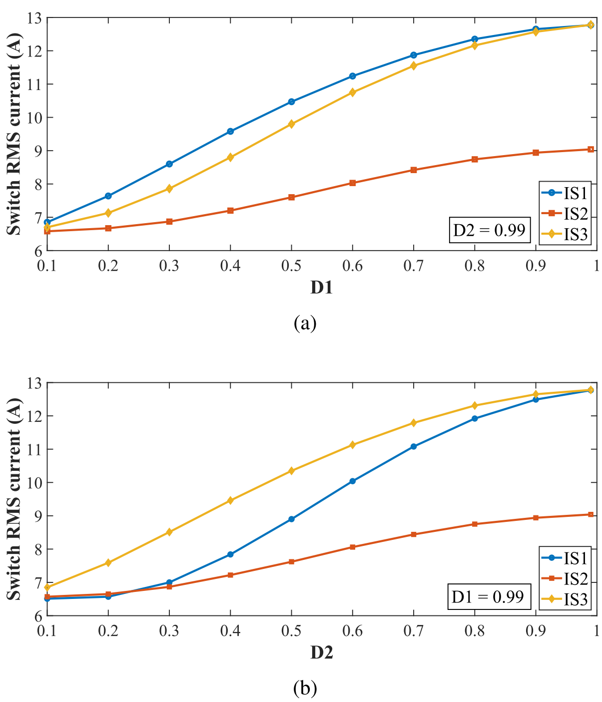

Fig. 6. Variation of switch rms current with duty cycle. (a) D_1 varied with D_2 constant at $D_{2\max}$. (b) D_2 varied with D_1 constant at $D_{1\max}$.

for the currents flowing through switch-1 (i_{S1}), switch-2 (i_{S2}), and switch-3 (i_{S3}) can be expressed as follows:

$$i_{S1} = \begin{cases} 0 & 0 < t < t_1 \\ i_{o1} & t_1 < t < t_2 \\ i_{o1} + i_{o2} & t_2 < t < T \end{cases} \tag{13}$$

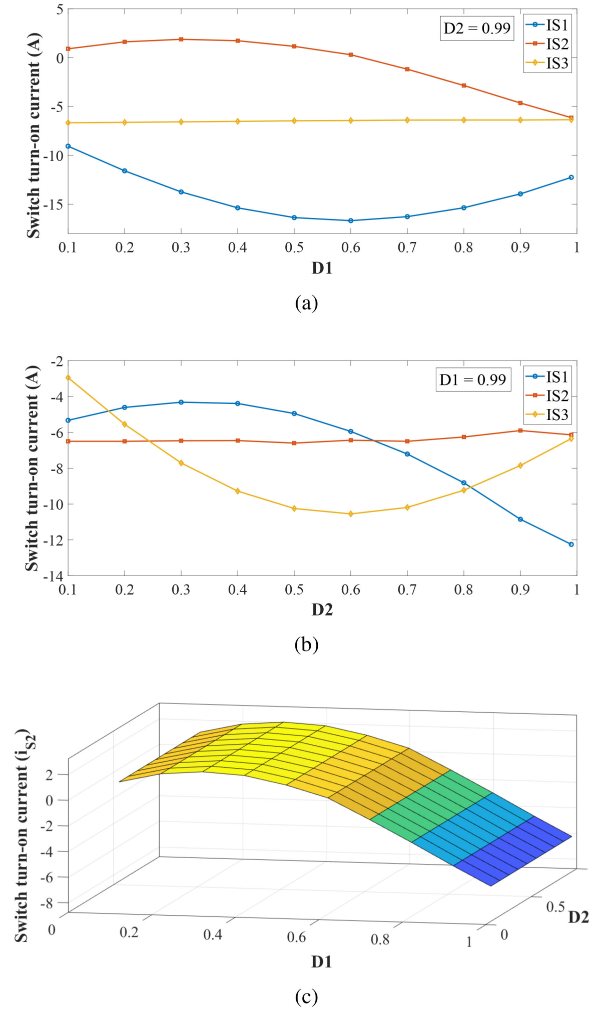

Fig. 7. Variation of switch turn-ON current with duty cycle. (a) D_1 varied with D_2 constant at $D_{2\max}$. (b) D_2 varied with D_1 constant at $D_{1\max}$. (c) Switch S_2 turn-ON current with variation in D_1 and D_2.

$$i_{S2} = \begin{cases} i_{o2} & 0 < t < t_1 \\ 0 & t_1 < t < t_2 \\ i_{o2} & t_2 < t < T \end{cases} \tag{14}$$

$$i_{S3} = \begin{cases} i_{o1} + i_{o2} & 0 < t < t_1 \\ i_{o2} & t_1 < t < t_2 \\ 0 & t_2 < t < T \end{cases} \tag{15}$$

where $t_1 = (1\text{-}D_1)$T and $t_2 = (1\text{-}D_2)$. Load currents can be expressed using expression (5) as follows:

$$i_{o1} = I_{m1} \sin(\omega t - \pi D_1 - \psi_1) \tag{16}$$

$$i_{o2} = I_{m2} \sin(\omega t - \pi D_2 - \psi_2) \tag{17}$$

where i_{o1} is load-1 current and i_{o2} is load-2 current. Instantaneous turn-ON and turn-OFF currents and rms currents for the devices can be obtained using (13) to (15). Conduction loss in switching devices can be expressed as follows:

$$P_{\text{con,sw}} = \left[(I_{S1})^2 + (I_{S2})^2 + (I_{S3})^2\right] \times r_{\text{DS}} \tag{18}$$

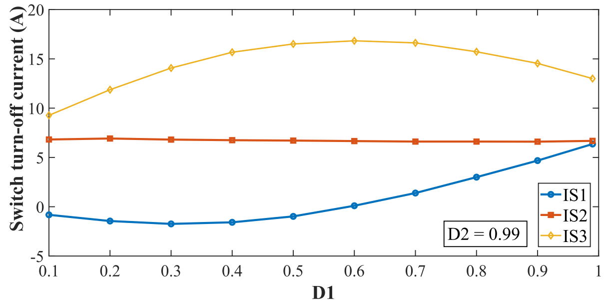

(a)

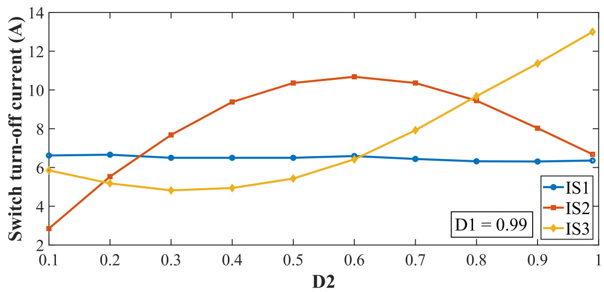

(b)

Fig. 8. Variation of switch turn-OFF current with duty cycle. (a) D_1 varied with D_2 constant at $D_{2\max}$. (b) D_2 varied with D_1 constant at $D_{1\max}$.

where $r_{\rm DS}$ is drain to source resistance of each MOSFET. I_{S1}, I_{S2}, and I_{S3} are rms currents flowing through switches S_1, S_2, and S_3, respectively. The variations in switch rms currents with duty cycle are shown in Fig. 6. Fig. 6(a) depicts change in switch rms currents when D_1 is varied by keeping D_2 at 99%. Fig. 6(b) shows the change in switch rms currents when D_2 is varied by keeping D_1 at 99%.

2) Conduction Losses in Resonant Capacitors and Induction Coil: Electrostatic resistance (ESR) of resonant capacitors will lead to conduction losses, which can be given as follows:

$$P_{\rm con,rc} = (I_{\rm rc,rms})^2 \times r_{\rm RC} \quad (19)$$

where $I_{\rm rc,rms}$ is the rms current flowing through the resonant capacitor, and $r_{\rm RC}$ is the ESR of resonant capacitor. The parasitic resistance of the IH coil also leads to losses, which is given as follows:

$$P_{\rm con,coil} = (I_{\rm coil,rms})^2 \times r_{\rm coil} \quad (20)$$

where $r_{\rm coil}$ and $I_{\rm coil,rms}$ are the resistance and rms current, which flows through the IH coil, respectively. In the proposed inverter, the current which flows through the resonant capacitors and the IH coil are same as the respective load currents.

B. Switching Losses

Switching losses are related to the turn-ON and turn-OFF of the devices. In the proposed 3SI, soft switching has been achieved for both the switching transitions of each device. Lagging nature of the load current ensures ZVS during turn-ON of the devices. The variation of switch turn-ON current with duty cycle is shown in Fig. 7. Fig. 7(a) depicts the change in switch turn-ON currents

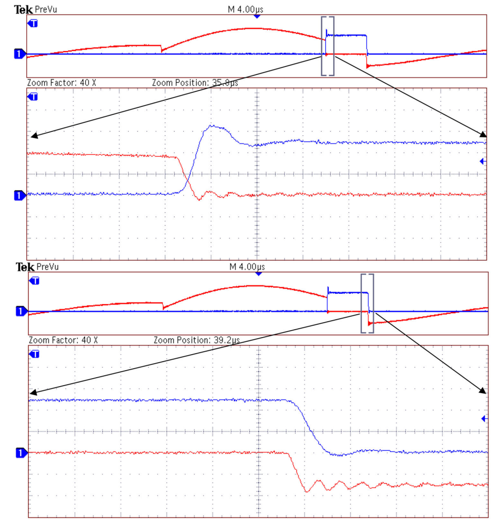
(a)

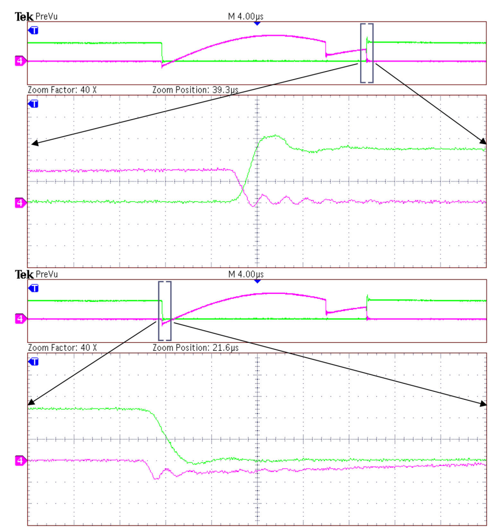
(b)

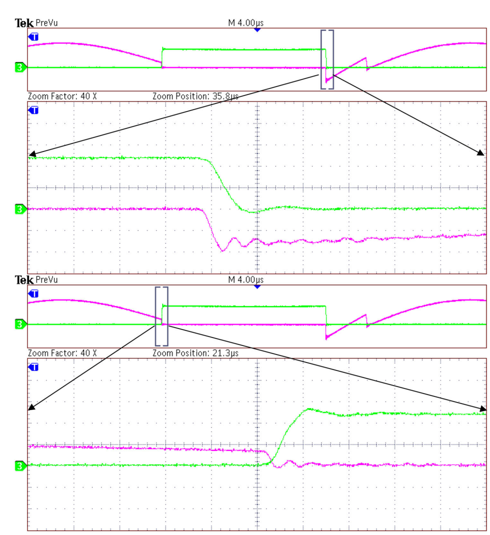
(c)

Fig. 9. Experimental voltage–current waveforms of switches. Turn-OFF and turn-ON transitions of switches (a) S_1 (b) S_2, and (c) S_3. Scale: Voltage (25 V/div), current (4 A/div), and time (100 ns/div).

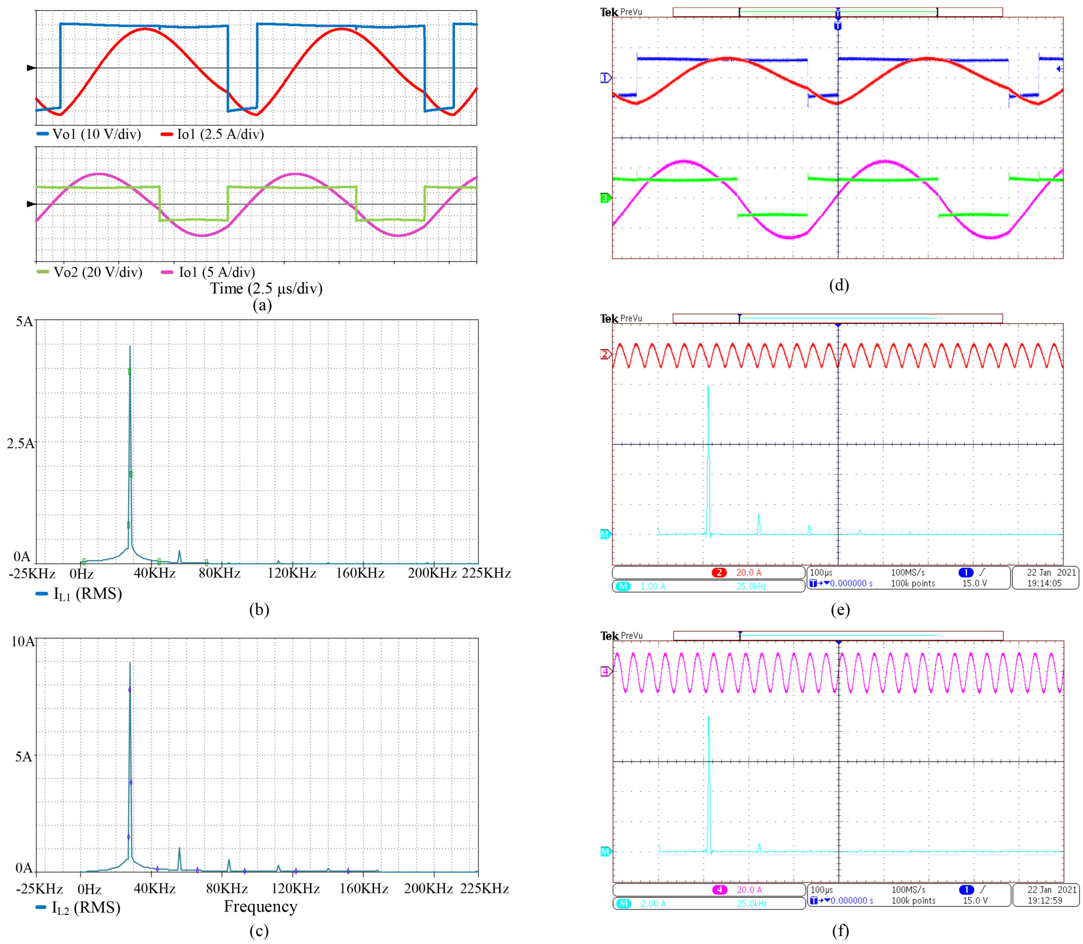

Fig. 10. Simulation and experimental results with $D_1 = 30\%$ and $D_2 = 70\%$. For load-1 and load-2: (a) Simulation waveforms of voltages and currents, (b), (c) FFTs for load currents under simulation, (d) experimental waveforms of voltages and currents (voltage: 50 V/div, current: 10 A/div), and (e), (f) FFTs for load currents under experimentation.

when D_1 is varied by keeping D_2 at 99%. Fig. 7(b) shows the change in switch turn-ON currents when D_2 is varied by keeping D_1 at 99%. Fig. 7(c) shows the variation of switch S_2 turn-ON current with duty cycles D_1 and D_2. The switch current has to be negative in order to ensure ZVS turn-ON of switches. The ZVS turn-ON range for the duty cycle can be observed from Fig. 7.

To ensure ZVS during turn-OFF, snubber capacitors C_s are connected across the drain-source terminal of each device and they are operated with a fixed deadtime t_{deadtime}. The criterion for the selection of the snubber and deadtime is given as follows:

$$t_{\text{snubber}} = \frac{V_{\text{dc}} C_s}{i_{\text{off}}} < t_{\text{dead-time}} < t_{\text{diode, min}}. \tag{21}$$

where t_{snubber} is the time for the snubber capacitor to reach V_{dc} voltage, $t_{\text{diode, min}}$ is the minimum diode conduction time, and i_{off} is the turn-OFF current. The variation of switch turn-OFF currents with duty cycle is shown in Fig. 8. Fig. 8(a) depicts change in switch turn-OFFcurrents when D_1 is varied by keeping D_2 at 99%. Fig. 8(b) shows the change in switch turn-OFF currents when D_2 is varied by keeping D_1 at 99%.

TABLE I
PARAMETERS OF THE PROPOSED 3SI

Component	**Value**
source voltages, $2 \times \frac{V_{\text{dc}}}{2}$	2×30 V
equivalent resistance of IH loads, $R_1 = R_2$	2.8 Ω
equivalent inductance of IH loads, $L_1 = L_2$	70.34 μH
resonant capacitors $C_{r1} = C_{r2}$ (MKV-B25834) (3×0.1 μF + 0.22 μF)	0.52 μF
ESR for 0.1 μF capacitor	33 mΩ
ESR for 0.22 μF capacitor	17 mΩ
parasitic resistance of IH coils	112 mΩ
switching frequency, f_{SW}	28 kHz
switching devices, MOSFETs	IRF540N
drain-source resistance of MOSFET, r_{DS}	40 mΩ

V. SIMULATION AND EXPERIMENTAL RESULTS

The proposed 3SI is simulated in Orcad PSpice software and verified experimentally with parameters given in Table I. The

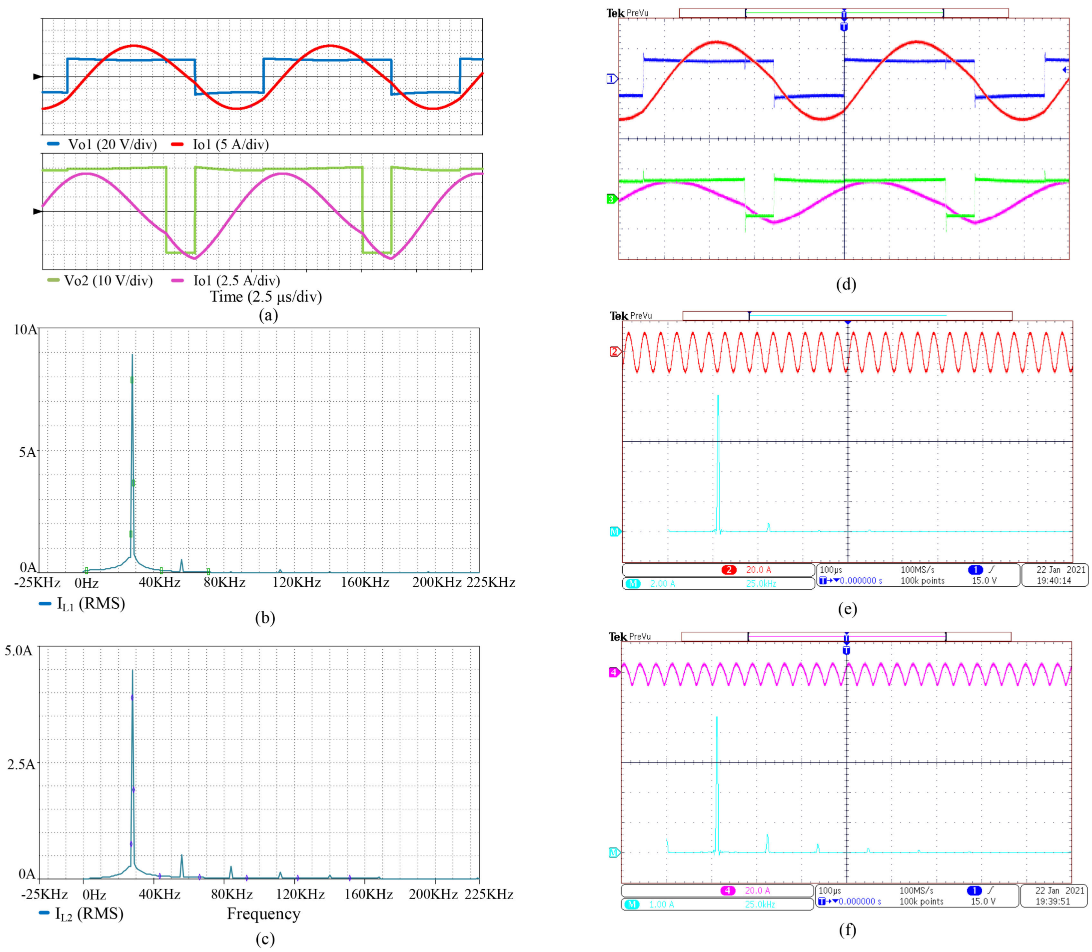

Fig. 11. Simulation and experimental results with $D_1 = 70\%$ and $D_2 = 30\%$. For load-1 and load-2: (a) Simulation waveforms of voltages and currents, (b), (c) FFTs for load currents under simulation, (d) experimental waveforms of voltages and currents (voltage: 50 V/div, current: 10 A/div), and (e), (f) FFTs for load currents under experimentation.

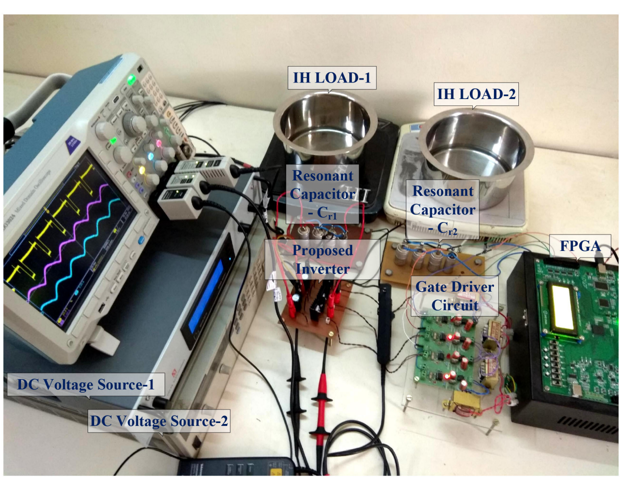

Fig. 12. Experimental setup.

complete experimental setup for the proposed 3SI is shown in Fig. 12. Although a single source with split capacitors can be used, two dc sources, Delta SM100-AR-75, and Agilent-35 V have been used for experimentation. In PV-based IH applications, dc sources can directly be obtained. A combination of steel vessel and an induction heating coil is realized as an IH load. It is modeled as an equivalent *RL* load. Two identical steel vessel loads are used for experimentation. Required capacitance to resonate each load is obtained by the series–parallel combination of MKV-type capacitors. The proposed 3SI is controlled using a field programmable gate array.

Independent power control in two IH loads is obtained using ADC control technique. The results for simulation and experimentation with duty cycle of load-1 as 30% and load-2 as 70% are shown in Fig. 10. Load-1 and load-2 are controlled at powers 56.7 and 222 W, respectively. Fig. 10(a)–(c) is shows the simulation results. Fig. 10(a) shows the voltage–current waveforms of IH loads. Fig. 10(b) and (c) shows the fast Fourier transforms (FFTs) for currents of respective loads. Fig. 10(d)–(f) shows the experimental results. Fig. 10(d) shows the voltage–current waveforms of IH loads. Fig. 10(e) and (f) shows FFTs for currents of respective loads.

Fig. 11 depicts the simulation and experimentation results with duty cycle of load-1 as 70% and load-2 as 30%. Load-1 and load-2 are controlled at powers 222 and 56.7 W, respectively. Fig. 11(a)–(c) shows the simulation results. Fig. 11(a) shows the

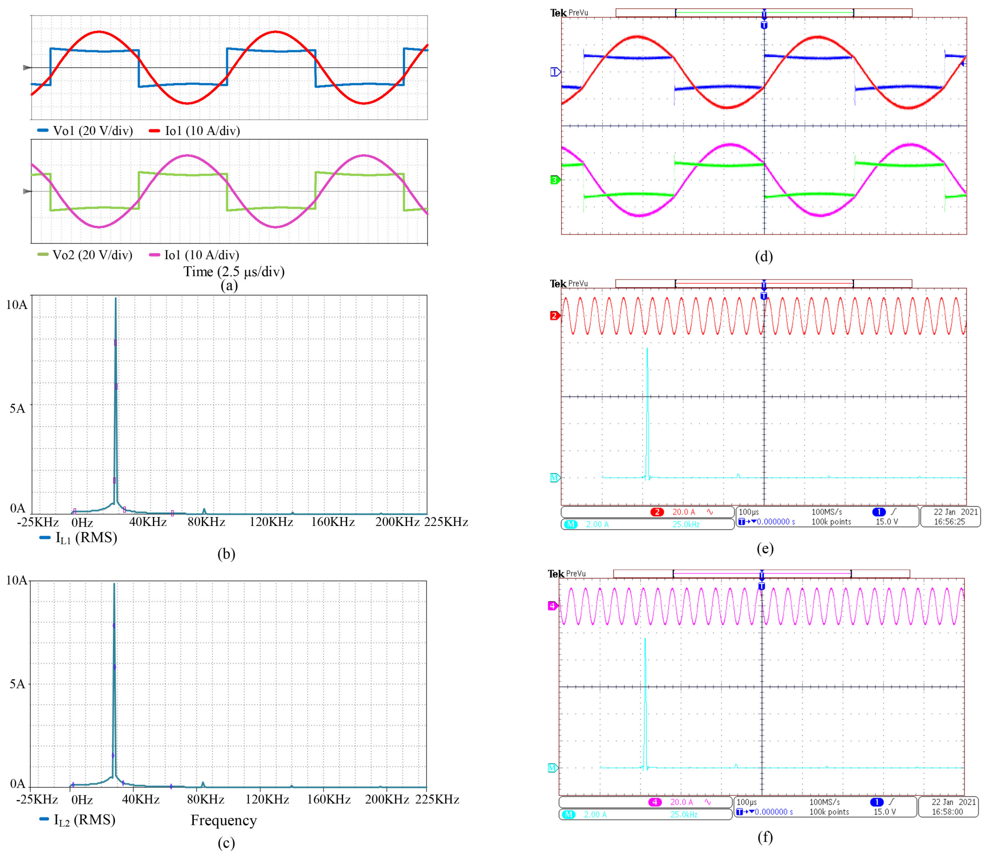

Fig. 13. Simulation and experimental results with $D_1 = D_2 = 99\%$. For load-1 and load-2: (a) Simulation waveforms of voltages and currents, (b), (c) FFTs for load currents under simulation, (d) experimental waveforms of voltages and currents (voltage: 50 V/div, current: 10 A/div), and (e), (f) FFTs for load currents under experimentation.

voltage–current waveforms of IH loads. Fig. 11(b) and (c) shows FFTs for load-1 and load-2 currents, respectively. Fig. 11(d)–(f), shows the experimental results. Fig. 11(d) shows the voltage–current waveforms of IH loads. Fig. 11(e) and (f) shows FFTs for currents of respective loads.

Fig. 13 depicts the simulation and experimentation results with duty cycle of 99% for both the loads. These two loads are operated at 275 W individually. Fig. 13(a)–(c), shows the simulation results. Fig. 13(a) shows the voltage–current waveforms of loads. Fig. 13(b) and (c) shows FFTs for currents of load-1 and load-2, respectively. Fig. 13(d)–(f) shows the experimental results. Fig. 13(d) shows the voltage–current waveforms of IH loads. Fig. 13(e) and (f) shows the FFTs for currents of, respective, loads.

From the abovementioned results, it can be perceived that simulation results are in harmony with the experimental results. It can be observed from FFTs that load currents contain fundamental component with negligible proportion of other harmonics. The experimental ZVS waveforms for the proposed 3SI is shown in Fig. 9. It can be observed that all three MOSFETs operates in ZVS. The experimental efficiency for variable load powers is calculated and is indicated in Fig. 14. The total system efficiency for the variation in load-1 power is calculated by keeping load-2 at constant maximum power and vice versa. Fig. 14(a) shows the efficiency of the system while power of load-1 is varied keeping load-2 constant at 275 W.

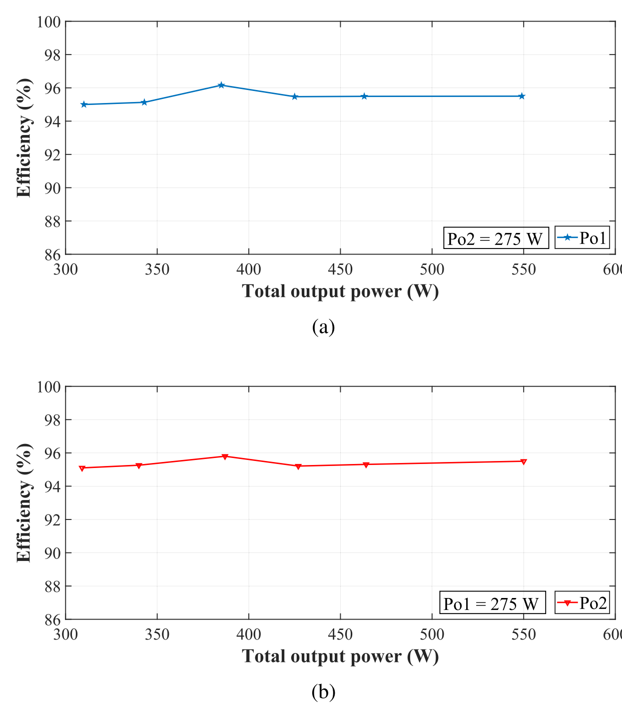

Fig. 14. Overall efficiency of the system with variation in total output power. (a) P_{o1} varied with P_{o2} constant at 275 W. (b) P_{o2} varied with P_{o1} constant at 275 W.

TABLE II
COMPARISON OF THE IH INVERTERS

Sr. No.	No. of switches and diodes	Operating frequency (kHz)	Soft switching	Peak efficiency (%)	Independent control	Simultaneous control	Switch to load ratio	Suitable for IH load material type
[14]	8	48	Yes	-	Yes	Yes	4	Ferromagnetic
[16]	6	30	Yes	95	No	Yes	2	Ferromagnetic
[19]	4	30,150	Yes	92	Yes	Yes	2	Ferro and non-ferromagnetic
[20]	5	25-125	Yes	96.5	Yes	No	5	Ferro and non-ferromagnetic
[21]	3	23-75	No	96	Yes	No	3	Ferro and non-ferromagnetic
[22]	8	20,100,400	No	≥92	Yes	Yes	2.67	Ferro and non-ferromagnetic
[23]	4	30/78	Yes	94.32	Yes	No	2	Ferro and non-ferromagnetic
Proposed 3SI	3	28	Yes	96.3	Yes	Yes	1.5	Ferromagnetic
Extension of the proposed 3SI	3	28 and 150	Yes	-	Yes	Yes	1.5	Ferro and non-ferromagnetic

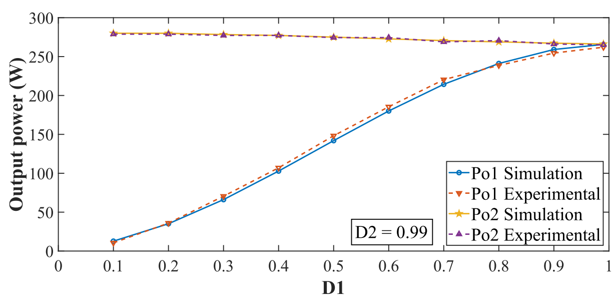

(a)

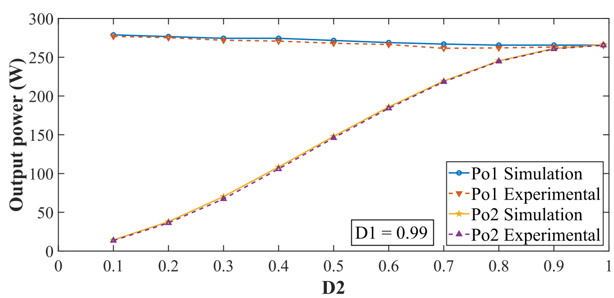

(b)

Fig. 15. Simulation versus experimental results of output power variation with duty cycle. (a) D_1 varied with D_2 constant at $D_{2\max}$. (b) D_2 varied with D_1 constant at $D_{1\max}$.

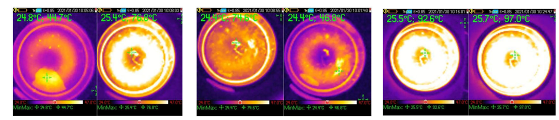

(a) (b) (c)

Fig. 16. Thermal images for different duty cycles for load-1 and load-2. D_1–D_2 combinations of (a) 30%–70%, (b) 70%–30%, and (c) 90%–90%.

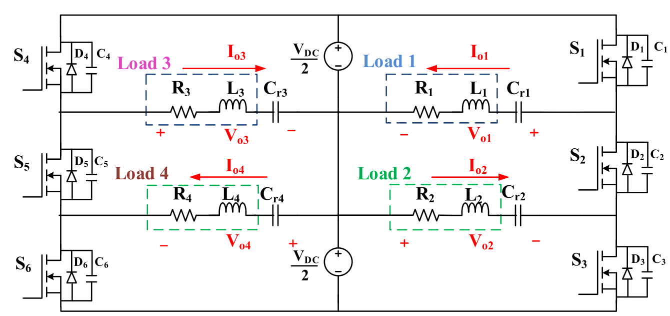

Fig. 17. Extension of the proposed 3SI.

Fig. 14(b) shows the efficiency of the system while load-2 power is varied with load-1 power maintained constant at 275 W. The proposed novel 3SI operates at greater than 95% efficiency over the entire range of operation with peak efficiency of 96.3%. Fig. 15 shows the simulation and experimental plots for output power variation as a function of duty cycle. Variation in load-1 power P_{o1} is plotted in Fig. 15(a), by maintaining duty cycle D_2 as constant at 99% and varying duty cycle D_1. Similarly, the variation in load-2 power P_{o2} is plotted in Fig. 15(b) by maintaining duty cycle D_1 as constant at 99% and varying duty cycle D_2. The simulation and the experimental results for output power variation with change in duty cycle are in accord with one another.

Fig. 16 shows thermal images of both the steel vessels, which are used as loads after powering them at different duty cycle for 1 min. Fig. 16(a) and (b) shows the thermal images for both the steel loads powered at 30%–70% and 70%–30% duty cycle combinations for 1 min. Fig. 16(c) shows the thermal images of both the loads operated at 90% duty cycle.

VI. Extension of the Proposed Inverter for Multiple Loads

The proposed configuration can be extended for multiple loads by adding a pair of three switches and two loads. Fig. 17 shows the extended configuration for four IH loads. Leg-1 with switches S_1, S_2, and S_3 can be used to control powers in load-1 and load-2. Leg-2 with switches S_4, S_5, and S_6 can be used to control powers in load-3 and load-4. Powers in each load can be independently controlled by using ADC control. Duty cycles of switches S_1, S_3, S_4, and S_6 control powers in load-1, load-2, load-3, and load-4, respectively. Each of these connected legs can be operated at different frequencies, which makes this topology suitable for heating magnetic as well as nonmagnetic materials.

VII. Conclusion

In this article, a 3SI configuration is proposed. Reduced number of components and high efficiency are the main benefits of the proposed inverter. ADC control technique is used to independently and simultaneously regulate powers in two loads. The 3SI has been analyzed, and analytical expressions for output current and power, power losses, and 3SI efficiency were derived. The 3SI operates at more than 95% efficiency over the entire range of operation and it offers peak efficiency of 96.3%. Also, it offers switch to load ratio of 1.5, which is lowest for multiload IH applications. The extension of the proposed inverter for more loads is possible with low switch to load ratio of 1.5. The extended topology has an added advantage of operating each leg at different frequencies, and this makes it suitable for heating magnetic as well as nonmagnetic materials. Comparison of the proposed 3SI with existing IH inverters is presented in Table II. The proposed 3SI offers compact and efficient solution to the multiload IH applications.

References

[1] H. N. Pham, H. Fujita, K. Ozaki, and N. Uchida, "Estimating method of heat distribution using 3-D resistance matrix for zone-control induction heating systems," *IEEE Trans. Power Electron.*, vol. 27, no. 7, pp. 3374–3382, Jul. 2012.

[2] S. Chudjuarjeen, A. Sangswang, and C. Koompai, "An improved *LLC* resonant inverter for induction-heating applications with asymmetrical control," *IEEE Trans. Ind. Electron.*, vol. 58, no. 7, pp. 2915–2925, Jul. 2011.

[3] M. Kamli, S. Yamamoto, and M. Abe, "A 50-150 kHz half-bridge inverter for induction heating applications," *IEEE Trans. Ind. Electron.*, vol. 43, no. 1, pp. 163–172, Feb. 1996.

[4] T. Mishima, C. Takami, and M. Nakaoka, "A new current phasor-controlled ZVS twin half-bridge high-frequency resonant inverter for induction heating," *IEEE Trans. Ind. Electron.*, vol. 61, no. 5, pp. 2531–2545, May 2014.

[5] J.-E. Yeon, K.-M. Cho, and H.-J. Kim, "A 3.6 kW single-ended resonant inverter for induction heating applications," in *Proc. 17th Eur. Conf. Power Electron. Appl.*, 2015, pp. 1–7.

[6] H. Sarnago, O. Lucia, A. Mediano, and J. M. Burdio, "Modulation scheme for improved operation of an RB-IGBT-based resonant inverter applied to domestic induction heating," *IEEE Trans. Ind. Electron.*, vol. 60, no. 5, pp. 2066–2073, May 2013.

[7] B. Saha, S. K. Kwon, N. A. Ahmed, H. Omori, and M. Nakaoka, "Commercial frequency AC to high frequency AC converter with boost-active clamp bridge single stage ZVS-PWM inverter," *IEEE Trans. Power Electron.*, vol. 23, no. 1, pp. 412–419, Jan. 2008.

[8] T. Ahmed, K. Ogura, S. Chandhaket, and M. Nakaoka, "Asymmetrical duty cycle controlled edge resonant soft switching high frequency inverter for consumer electromagnetic induction fluid heater," *Automatica, ATKAAF*, vol. 44, no. 1-2, pp. 21–26, 2003.

[9] V. Esteve *et al.*, "Improving the efficiency of IGBT series-resonant inverters using pulse density modulation," *IEEE Trans. Ind. Electron.*, vol. 58, no. 3, pp. 979–987, Mar. 2011.

[10] N. A. Ahmed, "High-frequency soft-switching AC conversion circuit with dual-mode PWM/PDM control strategy for high-power IH applications," *IEEE Trans. Ind. Electron.*, vol. 58, no. 4, pp. 1440–1448, Apr. 2011.

[11] Z. Ye, P. K. Jain, and P. C. Sen, "A full-bridge resonant inverter with modified phase-shift modulation for high-frequency AC power distribution systems," *IEEE Trans. Ind. Electron.*, vol. 54, no. 5, pp. 2831–2845, Oct. 2007.

[12] F. Forest, E. Laboure, F. Costa, and J. Gaspard, "Principle of a multi-load/single converter system for low power induction heating," *IEEE Trans. Power Electron.*, vol. 15, no. 2, pp. 223–230, Mar. 2000.

[13] T. Kominami and Y. Fujimoto, "A novel nine-switch inverter for independent control of two three-phase loads," in *Proc. IEEE Ind. Appl. Annu. Meeting*, 2007, pp. 2346–2350.

[14] J. Burdio, F. Monterde, J. Garcia, L. Barragan, and A. Martinez, "A two-output series-resonant inverter for induction-heating cooking appliances," *IEEE Trans. Power Electron.*, vol. 20, no. 4, pp. 815–822, Jul. 2005.

[15] S. Hosseini, A. Y. Goharrizi, and E. Karimi, "A multi-output series resonant inverter with asymmetrical voltage-cancellation control for induction-heating cooking appliances," in *Proc. CES/IEEE 5th Int. Power Electron. Motion Control Conf.*, 2006, vol. 3, pp. 1–6.

[16] P. Sharath Kumar, N. Vishwanathan, and B. K. Murthy, "Multiple-load induction cooking application with three-leg inverter configuration," *J. Power Electron.*, vol. 15, no. 5, pp. 1392–1401, 2015.

[17] V. B. Devara, V. Neti, T. Maity, and P. Shunmugam, "Capacitor-sharing two-output series-resonant inverter for induction cooking application," *IET Power Electron.*, vol. 9, no. 11, pp. 2240–2248, 2016.

[18] W. Meesrisuk, A. Jangwanitlert, and W. Suwan-ngam, "Implementation of two-output three-level series-resonant inverter for induction melting application," *IET Power Electron.*, vol. 11, no. 1, pp. 129–139, 2018.

[19] S. K. Papani, V. Neti, and B. K. Murthy, "Dual frequency inverter configuration for multiple-load induction cooking application," *IET Power Electron.*, vol. 8, no. 4, pp. 591–601, 2015.

[20] H.-P. Park and J.-H. Jung, "Load-adaptive modulation of a series-resonant inverter for all-metal induction heating applications," *IEEE Trans. on Ind. Electron.*, vol. 65, no. 9, pp. 6983–6993, Sep. 2018.

[21] I. Millan, J. Burdío, J. Acero, O. Lucía, and S. Llorente, "Series resonant inverter with selective harmonic operation applied to all-metal domestic induction heating," *IET Power Electron.*, vol. 4, no. 5, pp. 587–592, 2011.

[22] S. Khatroth and P. Shunmugam, "Cascaded full-bridge resonant inverter configuration for different material vessel induction cooking," *IET Power Electron.*, vol. 13, no. 19, pp. 4428–4438, 2020.

[23] W. Han, K. T. Chau, W. Liu, X. Tian, and H. Wang, "A dual-resonant topology-reconfigurable inverter for all-metal induction heating," *IEEE J. Emerg. Sel. Top. Power Electron.*, early access, Apr. 2021, doi: 10.1109/JESTPE.2021.3071700.

Bhavin Salvi received the B.E. degree in electrical engineering from Birla Vishwakarma Mahavidyalaya, Gujarat, India, in 2013 and the M.Tech. degree in power electronics and drives in 2018 from the National Institute of Technology Warangal, Warangal, India, where he is currently working toward the Ph.D. degree.

His main research interests include power electronics converter development and digital control for induction heating system, LED lighting system, and maximum power point tracking in photovoltaic based applications.

S. Porpandiselvi (Member, IEEE) received the B.E. degree in electrical and electronics engineering from the Thiagarajar College of Engineering, Madurai, India, in 1996, the M.E. degree in applied electronics from Madurai Kamaraj University, Palkalai Nagar, India, in 2001, and the Ph.D. degree in electrical engineering from the National Institute of Technology Warangal, Warangal, India, in 2014.

She is currently an Assistant Professor with th Department of Electrical Engineering, National Institute of Technology Warangal. Her research interests include high frequency inverters for induction heating applications, Resonant converters, LED driver circuits, and PV based applications.

N. Vishwanathan received the B.Sc. (Engg.) degree in electrical engineering from Dayalbagh Educational Institute, Agra, India, in 1990, the M.Tech. degree in electrical machines and industrial drives from Regional Engineering College Warangal, Warangal, India, in 1992, and the Ph.D. degree from the Indian Institute of Science, Bangalore, India, in 2004.

He is currently a Professor with the Department of Electrical Engineering, National Institute of Technology Warangal, Warangal, India. His research interests include switched mode power conversion, LED lighting, and electrical drives.